

# Clark Y-14 Airfoil Analysis

02/28/03

Giancarlo Bruschi, Tomoko Nishioka, Kevin Tsang, Rick Wang

## **Abstract**

Airfoils have become an integral aspect of human flight as it has evolved over the last century. As the design of each airfoil determines many aspects of its use in the real world, all significant characteristics must be analyzed prior to implementation. The aerodynamic effects of pressure, drag, lift, and pitching moment were used to evaluate the behavior of the Clark Y-14 airfoil. In this experiment, pressure distribution was recorded over the upper and lower surfaces of the airfoil and compared to theoretical values created by Visual Foil, a computer simulation package. In the same respect, wake pressure measurements were taken directly downstream of the airfoil to determine the loss of momentum, and in turn the drag force on the Clark Y-14. The lift, drag, and pitching moment were then recalculated using data recorded through the use of a force balance. From the results it was concluded that the theoretical and measured data exhibit strong agreement throughout the three methods.

# Contents

<b>1</b>	<b>Introduction</b>	<b>5</b>
1.1	History of Aviation .....	5
1.2	Modern Day Aviation .....	6
1.3	Wind Tunnel Experiments .....	7
1.4	Characterizing the Clark Y-14 .....	8
<b>2</b>	<b>Theory</b>	<b>9</b>
2.1	Aerodynamic Forces .....	9
2.2	Low-Speed Aerodynamics .....	10
2.3	Characterizing Airfoil Performance .....	11
2.4	Obtaining Airfoil Characteristics from Data .....	12
2.4.1	Airfoil Control Volume Analysis .....	12
2.4.2	Test Section Control Volume Analysis .....	13
2.4.3	Airfoil Direct Force Measurement .....	14
<b>3</b>	<b>Procedure</b>	<b>16</b>
3.1	Calibration of the Wind Tunnel .....	16
3.2	Pressure Distribution over Airfoil .....	16
3.3	Force Balance Analysis .....	17
<b>4</b>	<b>Results</b>	<b>18</b>
<b>5</b>	<b>Discussion</b>	<b>20</b>
5.1	Pressure Coefficients and Chord Length .....	20
5.2	Lift Coefficients and Drag Coefficients vs. Angle of Attack .....	21

5.3	Pitching Moment Coefficients .....	22
5.4	Center of Pressure .....	23
5.5	Pitching Moment through the Quarter Chord Point.....	23
5.6	Wake Survey Pressure Distribution of Vertically mounted Pressure Wing .....	23
5.7	Drag Coefficient from the Momentum Method.....	24
5.8	Effect of Reynolds Number on Lift, Drag, and $\frac{1}{4}$ Chord Pitching Moment.....	24
5.9	Interpretation of Sting Balance Data.....	25
5.9.1	Lift.....	25
5.9.2	Drag.....	25
<b>6</b>	<b>Conclusion</b>	<b>27</b>
<b>7</b>	<b>References</b>	<b>28</b>
<b>8</b>	<b>Error Analysis</b>	<b>29</b>
8.1	Calibration.....	29
8.2	Pressure Distribution.....	31
8.3	Wake Survey .....	33
8.4	Force Balance.....	34
<b>9</b>	<b>Appendix</b>	<b>37</b>
<b>List of Figures</b>		
Figure 1	Airfoil Nomenclature [2].....	7
Figure 2	Aerodynamic forces.....	10
Figure 3	Pressure distribution over airfoil [1].....	13
Figure 4	Control volume on a 2-D body [2] .....	14

Figure 5 Schematic of forces on sting balance [1].....	15
Figure 6 .....	37
Figure 7 .....	38
Figure 8 .....	38
Figure 9 .....	39
Figure 10 .....	39
Figure 11 .....	40
Figure 12 .....	40
Figure 13 .....	41
Figure 14 .....	41
Figure 15 .....	42
Figure 16 .....	42
Figure 17 .....	43
Figure 18 .....	43
Figure 19 .....	44
Figure 20 .....	44
Figure 21 .....	45
Figure 22 .....	45

# 1 Introduction

## 1.1 History of Aviation

The earliest attempts to achieve human flight were characterized by failures in converting the motion of birds into mechanical flight. Although these attempts were unsuccessful, the early

experimenters made the important discovery that aerodynamic forces were a function of relative velocity. Researchers began to develop innovative experiments and formulate new theories in an effort to understand the physics that would unlock the secret to powered flight. One of the more significant experiments to emerge was the Wright brothers' wind tunnel, which enabled them to test a variety of wing profiles in rapid succession. These wing profiles, known as *airfoils*, are shapes that provide a buoyant force by inducing a pressure gradient. With this valuable tool to evaluate the performance of various airfoils, the Wright brothers were able to debunk contemporary theory and invent the first human powered flying machine [1].

## **1.2 Modern Day Aviation**

Today, airfoils are continuously re-evaluated in order to meet the growing demand in commercial, military, and scientific applications. Drag can be reduced to save on fuel costs; lift can be increased to enable lower speed flight; profiles can be redesigned to accommodate heat transfer at high speeds. In these applications, airfoils are optimized for performance and economy at specific operating conditions defined by altitude, temperature, and velocity.

The main consideration in airfoil design is the relative velocity of the airfoil. For this reason, airfoils for subsonic, transonic, supersonic, and hypersonic flow conditions exhibit strikingly different design philosophies [2]. High speed airfoils may have less camber to reduce skin friction drag and low speed airfoils will tend to have more camber in order to maximize lift. Different airfoils are defined by various parameters such as leading edge (LE), trailing edge (TE), thickness ( $t$ ), chord ( $c$ ), and camber, as seen in Figure 1.

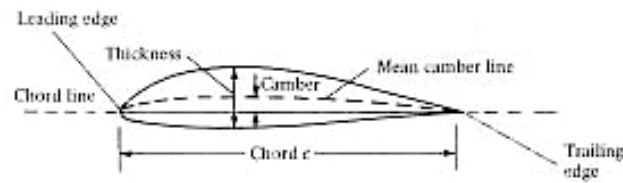


Figure 1: Airfoil Nomenclature [2]

### 1.3 Wind Tunnel Experiments

The wind tunnel experiment may be conducted in a variety of setups. For example, the airfoil may be positioned in a different manner to allow either 2D or 3D air flow. In a 2D experiment, a uniform airfoil profile would be either mounted directly to the wall or to an endplate insert. In this arrangement, the fluid flow over the wingspan is uniform in the span-wise direction. However, in a 3D experiment, the wing profile or prototype model would be mounted to a strut or sting and centered in the wind tunnel to allow flow interaction at the wing tips. The analysis of 2D results would give the researcher insight into the profile, and the 3D results will more closely resemble actual operating conditions.

In either setup, experimental data may be collected in the form of pressure, force, or moment measurements. Unfortunately, variables of interest such as lift and drag may not be measured directly. Consequently, indirect measurements can be obtained by measuring the pressure distribution over the wing, performing a force balance, or analyzing the effects of balance alignment and aspect ratio<sup>1</sup>. Each experimental setup is sensitive to a specific set of idealizations, and it is worthwhile to collect data from a variety of setups in order to obtain

<sup>1</sup> A more comprehensive description of low-speed wind tunnel experiments may be found in [1].

accurate results. From these results, the airfoil may be characterized by obtaining values for the coefficients of drag ( $C_D$ ), lift ( $C_L$ ), moment ( $C_M$ ), and normal force ( $C_N$ ). Other values such as stall ( $\alpha_{L=0}$ ) and center of pressure ( $X_{CP}$ ) may be calculated as well. These values are reasonable indicators of actual airfoil performance.

#### **1.4 Characterizing the Clark Y-14**

The airfoil chosen for this experiment was the Clark Y-14, a general purpose airfoil used for its superb control at low Reynolds numbers. An additional feature of this airfoil is that its lower surface is parallel to its chord and this enables the use of an inclinometer to change the angle of attack directly. In this experiment, Clark Y-14 airfoil is characterized under low-speed operating conditions. A full length profile is vertically mounted in the wind tunnel to obtain 2D flow conditions and pressure distributions over the chord and the wake are measured. In addition, a 3D flow experiment was conducted by mounting a short airfoil to a sting balance, in a horizontal position, to measure reaction forces directly. The data obtained from both experiments was then analyzed in order to obtain values for the coefficients  $C_L$ ,  $C_D$ ,  $C_M$  and  $C_N$ . The pitching moments, center of pressure, and stall were also calculated. These results were then compared to theoretical data obtained by computer simulation to build a more rigorous analysis of the Clark Y-14 airfoil's behavior under low speed conditions.

## 2 Theory

### 2.1 Aerodynamic Forces

The aerodynamic forces acting on a body may be described by *lift*, *drag*, and *pitching moment*. *Lift* is the net vertical force and *drag* is the net horizontal force with respect to the direction of motion. The *pitching moment* reflects the tendency of the airfoil to pitch about a given reference point. These quantities are derived from the normal force and axial force acting on the airfoil by trigonometric relations (Eq. (1)).

$$\begin{aligned} F_L &= N \cos \alpha - A \sin \alpha \\ F_D &= A \cos \alpha + N \sin \alpha \end{aligned} \quad (1)$$

The normal force (N) is defined as the force perpendicular to the airfoil chord and the axial force (A) is the force acting parallel to the chord. It can be seen in these equations that the lift force ( $F_L$ ) and drag force ( $F_D$ ) are both derived from the same normal and axial force. However, the angle of attack ( $\alpha$ ) determines how much of the normal and axial forces transfer into lift and how much into drag. The pitching moment may be expressed by an integral of the net moments acting on the airfoil (Eq. (2)).

$$M = \int_{LE}^{TE} dM_u + \int_{LE}^{TE} dM_L \quad (2)$$

In this equation, the differential moments are taken with respect to a given reference and then integrated from the leading edge to the trailing edge. A graphical representation of these forces is shown in Figure 2.

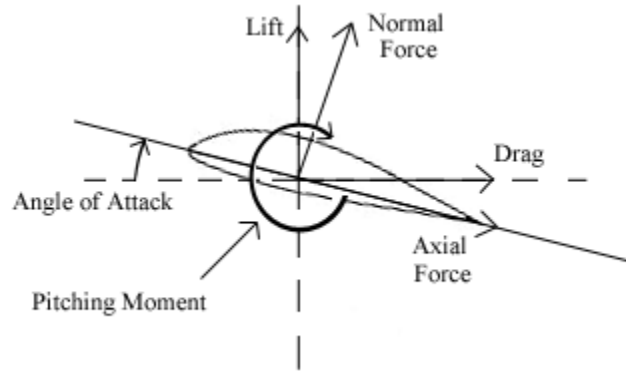


**Figure 2: Aerodynamic forces**

## 2.2 Low-Speed Aerodynamics

In low-speed flows, where the free stream velocity is well under Mach 0.3, several idealizations may be applied to simplify fluid dynamics analysis. One such idealization was that the air density was assumed constant since it varies by only a few percent from speeds of 0 to 300 mph. This idealization is known as *incompressible flow* [2]. Another idealization, *inviscid flow*, was made by neglecting viscous effects such as friction, thermal conduction, and diffusion<sup>2</sup>. Such effects are known to be minimal for low-speed air flow and this idealization is well supported by current theory. The flow was assumed to be steady, and the body forces acting on the working fluid were assumed to be minor compared to dynamic effects. These idealized conditions are sufficient to allow the use of Bernoulli's equation, Eq. (3), in low-speed flow analysis [2].

Bernoulli's equation may also be derived from the momentum equation by considering a differential control volume and applying the assumptions made previously<sup>3</sup>. The resulting

<sup>2</sup> Viscous effects are significant at low Reynolds numbers and addressed in [3]

<sup>3</sup> This derivation is covered in detail in [3]

equation shows that the sum of the local pressure ( $p$ ) and dynamic pressure (Eq. (4)) are constant throughout a given flow. From this equation, the local velocities may be computed from knowledge of upstream data and local pressure so that all of the flow characteristics may be obtained.

$$p + \frac{1}{2} \rho V^2 = \text{constant} = p + q_\infty \quad (3)$$

$$q_\infty = \frac{1}{2} \rho V_\infty^2 \quad (4)$$

Effects of the wind tunnel walls may be ignored by applying the inviscid flow approximation. By doing so, the flow may be assumed to be uniform except over the airfoil. Uniform flow simplifies control volume analysis, and allows the consideration of a full length airfoil as a 2D profile [3]. The assumption of uniform flow is justified due to the smooth wind tunnel walls, the filtered flow, and the controlled entry flow into the test section.

### **2.3 Characterizing Airfoil Performance**

Airfoil performance may be characterized by quantities such as the lift, drag or pitching moment produced under different operating conditions. These aerodynamic forces are often computed from the total pressure over the planform area, and then normalized by the dynamic pressure in order to produce non-dimensional quantities. For example, the lift coefficient may be expressed as Eq. (5) [3]. The drag and normal force coefficients may also be expressed in a similar manner as Eq. (6) and Eq. (7). The pitching moment must also be normalized by the chord length in order to produce a non dimensional moment coefficient Eq. (8).

$$C_L \equiv \frac{F_L}{\frac{1}{2} \rho_\infty V_\infty^2 A} \quad (5)$$

$$C_D \equiv \frac{F_D}{\frac{1}{2} \rho_\infty V_\infty^2 A} \quad (6)$$

$$C_N \equiv \frac{F_N}{\frac{1}{2} \rho_\infty V_\infty^2 A} = \frac{p}{q_\infty} \quad (7)$$

$$C_M \equiv \frac{\int \Delta p(x) dc}{q_\infty c} = \frac{M}{\frac{1}{2} \rho_\infty V_\infty^2 A c} \quad (8)$$

These non-dimensional quantities are functions of the Reynolds number and the angle of attack. The Reynolds influence may be seen by the inclusion of the density ( $\rho_\infty$ ) and velocity ( $V_\infty$ ) terms, while the angle of attack influence is implied through the force, moment and area terms. Thus, in order to appreciate the full range of responses of a given airfoil, it is necessary to consider a range of Reynolds numbers and angles of attack. Variation in the Reynolds number produces different lift curves, while variations in the angle of attack will alter the lift-drag ratio.

## 2.4 Obtaining Airfoil Characteristics from Data

### 2.4.1 Airfoil Control Volume Analysis

One method of obtaining the lift, drag, and pitching moment coefficients of interest is to analyze a control volume over the surface of the airfoil. In this method, localized pressure measurements are taken in a plane in the chord wise direction on both the upper and lower surfaces to obtain a

pressure distribution Figure 3. The difference in the pressure distributions may then be integrated in order to obtain an expression for the net pressure acting over the surface.

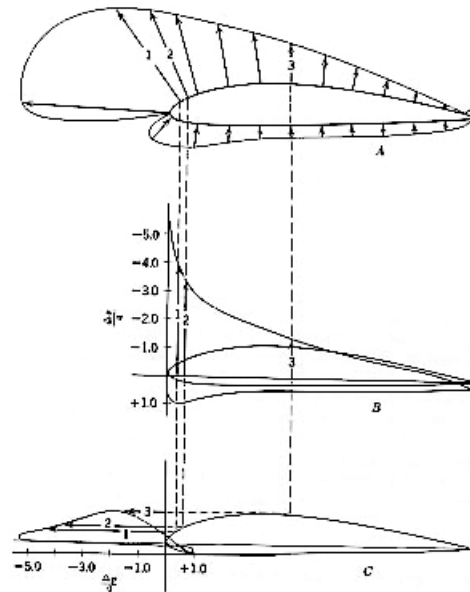


**Figure 3: Pressure distribution over airfoil [1]**

In the pressure distribution shown in Figure 3, the arrows pointing towards the wingspan represent a positive gage pressure while the upper pressure distribution shows outward pointing arrows to show negative gage pressure. This is clarified in the two plots shown below the pressure distribution diagram. It can be seen that the normalized gage pressure is lowest near the leading edge where the velocity is the highest. This observation confirms the behavior predicted by Bernoulli's equation (Eq.(3)). However, a limitation of this arrangement is that the summation of pressure data fails to detect the axial forces acting on the airfoil and the skin friction is unaccounted for.

#### **2.4.2 Test Section Control Volume Analysis**

An alternative method of measuring drag force is to perform a control volume analysis over a streamline bounded control volume. By applying conservation of momentum to this control

volume, it can be deduced that the body within the control volume contributed to a loss of momentum. This effect may be visualized by marking the inlet and outlet velocity profiles as shown in Figure 4. The inlet flow is uniform, while the outlet flow will have a non-uniform shape due to localized loss of momentum.

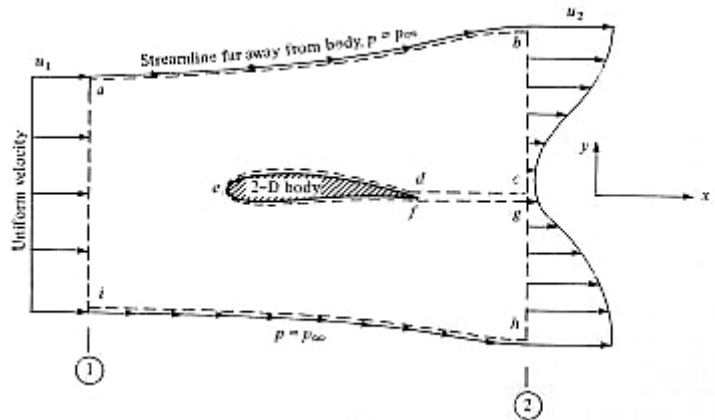


**Figure 4: Control volume on a 2-D body [2]**

This loss of momentum is known as the drag produced by the airfoil, and may be indirectly calculated by solving the velocity profiles at either end of the control volume. Alternatively, through the use of Bernoulli's equation (Eq. (3)), localized pressure measurements in the wake may be used instead. A non-dimensional analysis considering normalized pressure was then used to solve the coefficient of drag. This type of arrangement will provide sufficient data to calculate the drag coefficient, but differential forces were not measured and thus lift and moment cannot be evaluated from this data.

### 2.4.3 Airfoil Direct Force Measurement

A more realistic method of predicting airfoil performance is to consider a finite length wingspan mounted in the center of the test section. The 3D of arrangement uses a sting balance that measures the axial and normal reaction force imposed on the sting-airfoil structure due to the

flow Figure 5. The reduced constraints allow the airfoil to respond with the full six degrees of freedom, and the finite width of the airfoil will allow rotational flow over the sides of the wings.

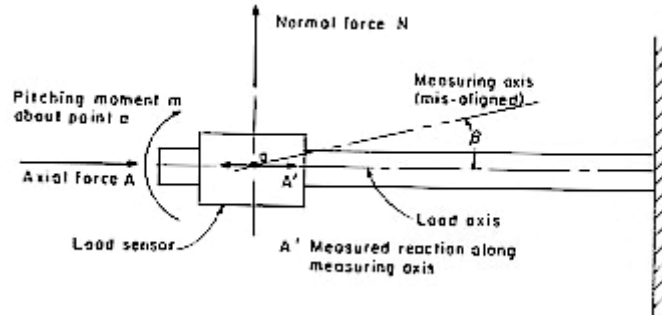


Figure 5: Schematic of forces on sting balance [1]

Measured quantities may be transferred into forces acting on the wing by a series of empirical correlations, where  $N'$ ,  $A'$ , and  $P'$  denote the normal force, axial force, and pitching moment as measured by the sting balance (Eq. (9)).

$$\begin{aligned}
 N &= .9504N' - .0082A' - .0161P' \\
 A &= .0608N' + .5912A' \\
 P &= -.1336N' + .0119A' + 1.182P'
 \end{aligned}
 \tag{9}$$

These values may then be used to solve for lift and drag through simple geometry, by breaking the normal and axial forces into components along and perpendicular to the airfoil chord (Eq. (1)). The geometry of the wing is then accounted for by nondimensionalizing these values (Eq. (5)) to obtain the various aerodynamic coefficients.

### **3 Procedure**

All experiments were carried out at the University of California, San Diego Mechanical Engineering Undergraduate Laboratory. The wind tunnel used for this experiment was a small, low speed open return system. In all tests, the Clark Y-14 airfoil was analyzed in a test section, equipped with all necessary pressure measurement and force balance equipment for the data retrieved.

#### **3.1 Calibration of the Wind Tunnel**

Prior to the experiment, calibration of the wind tunnel was performed to provide accurate measurements on that specific day. The air pressure and temperature were recorded from the manometer and thermometer located inside the wind tunnel. From these values, the Reynolds number was obtained for the ambient air. The pitot tube pressure in inches of water was recorded by the Wind Tunnel Calibration Virtual Instrument (VI). In this VI, each pressure reading was taken from motor frequencies ranging from 0 to 60 Hz, in increments of 5 Hz. The pressure readings were converted to velocity by the use of Bernoulli's equation. A trendline was fitted to the plot of air velocity vs. motor frequency. From this trendline, the motor frequencies corresponding to the desired velocities were computed.

#### **3.2 Pressure Distribution over Airfoil**

The Clark Y-14 airfoil was positioned vertically in the test section of the wind tunnel during the pressure distribution experiment. The pressure tubes mounted in the airfoil and rake were connected to the inlets of the multiplexed tunnel pressure sampling system. The static pressure of the test section was connected to the reference connection of the pressure transducer. From these

measurements, the coefficient of pressure was determined. Before the measurements can be taken for the desired air velocities, the Pressure Distribution VI was used to record the zero velocity pressure measurements. All the amplifiers were set to zero prior to running this VI. Once the zero velocity pressure measurements were recorded, they were used as a reference to correct the offset in the recorded data. The pressure coefficients for the vertical airfoil were obtained at three different airspeeds: 80, 100, and 120 mph, at for the four angles of attack of -4 degrees, 0 degrees, 4 degrees, and 8 degrees. All data were automatically recorded by the program.

### **3.3 Force Balance Analysis**

For the force balance experiment, a Clark Y-14 airfoil was mounted horizontally in the test section of the wind tunnel. As with the pressure distribution experiment, calibration of the wind tunnel was first completed to find the corresponding motor frequency to each velocity. Once this is completed, a LabVIEW program, the Sting VI was used to obtain normal force, axial force, and pitching moment. Readings of these forces were taken from -6 degrees at 2 degrees intervals to 20 degrees. The angle of attack was varied by controlling the inclinometer connected to the force balance. Airspeed was held constant at 80 mph while the angle of attack is incremented through the testing range. Each data point was recorded digitally by pressing the scan button on the Sting VI which was taken approximately 10-15 sec after the angle of attack had been moved in order to allow time for the instrument to stabilize. The first set of data was recorded at zero velocity to account for the offset, which is subtracted off from later readings. This same procedure was then repeated at speeds of 100 and 120 mph. All data recorded by the VI were saved as files for later analysis.

## 4 Results

The pressure distribution measurements provided quantitative data to determine the drag, lift, moment, and pressure coefficients as well as the center of pressure. One of the initial values needed to compute was the pressure coefficient,  $C_P$ , over the upper and lower surfaces of the Clark Y-14 airfoil through a range of angle of attack. The upper and lower pressure coefficient at each data point along the chord was calculated by normalizing the gage pressure by the free stream dynamic pressure. These values were then tabulated and plotted in Figure 6, Figure 7, Figure 8, and Figure 9. The difference of these values was then computed to obtain a value of  $C_N$  for that data point. To compute the value of the total  $C_N$ , the individual  $C_N$  at each data point were summed according to the trapezoidal rule (Eq. (10)).

$$C_{N,total} \approx \sum_i \frac{[C_{N,i} + C_{N,i+1}][x_i + x_{i+1}]}{2} \quad (10)$$

In this equation  $x_i$  represents the position of each pitot probe along the chord of the airfoil, and  $C_N$  represents the local normal force coefficient at that data point. The total  $C_N$  was split into components  $C_L$  and  $C_D$  by trigonometric relations (Eq. (1)) with omission of the axial force. These coefficients are tabulated in Table 1 and plotted against angle of attack in Figure 10 and Figure 11.

The pitching moment coefficient about the leading edge and the quarter chord point were calculated by a trapezoidal approximation as well (Eq. (11)). In addition, the moment was approximated by taking the midpoint between data points to represent the term  $x-x_{ref}$  in the previous equation to obtain Eq. (12).

$$C_{M,refl} \approx \sum_i \frac{[C_{N,i} + C_{N,i+1}][x_i + x_{i+1}]}{2} [x - x_{ref}] \quad (11)$$

$$C_{M,ref} \approx \sum_i \frac{[C_{N,i} + C_{N,i+1}][x_i + x_{i+1}]}{2} [\bar{x}] \quad (12)$$

The resulting values of  $C_M$  are tabulated in Table 1. The pitching moment coefficient about the leading edge was used to solve for the center pressure (Eq. (13)).

$$\frac{X_{cp}}{c} = -\frac{C_{M,LE}}{C_N} \quad (13)$$

The pitching moment coefficient about the quarter chord was calculated and plotted as a function of angle of attack for each velocity. The results of the above calculations are also in Table 1 and Figure 20. All experimental values were tabulated alongside Visual Foil predictions for comparison.

## 5 Discussion

### 5.1 Pressure Coefficients and Chord Length

The upper surface of the airfoil is concave, while the lower surface is relatively flat. Considering the geometry of the airfoil, it can be clearly seen that the upper surface has a much larger surface area than that of the lower surface. As a result, the wind flow on upper surface must travel faster than the flow on the lower surface. As the air flow travels from 0% to 100% chord, the flow separates onto the lower and upper surfaces.

Figure 6, Figure 7, Figure 8, and Figure 9 shows the distribution of the pressure coefficient of the upper and lower surfaces versus the distance of percentage chord length. Each plot represents one angle of attack for three different wind speeds. From the trapezoidal rule, the calculated values of the normal force coefficient,  $C_N$  were calculated and are shown in **Error! Reference source not found.** From the data, it seems that the value of  $C_N$  was fairly consistent as velocity was varied. This demonstrates that the normal force coefficient is independent of the Reynolds Number at the ranges tested. Another trend seen in these values was that the value of  $C_N$  increases as the angle of attack is increased.

Experimental data was compared to theoretical values obtained by the Visual Foil software. The computer simulator generates a pressure coefficient distribution for the upper and lower surfaces of an airfoil for different air speeds and angles of attack. These values are plotted along with the experimental pressure coefficient data obtained from the airfoil in Figure 6, Figure 7, Figure 8, and Figure 9. In comparison to the experimentally obtained pressure coefficient data, the distribution given by Visual Foil characterizes the experimentally obtained data to a degree, except for low chord percentages of less than approximately 20% chord. This small variance will

lead to differences in the calculated and theoretical values of several aerodynamic coefficients. This error was recovered when two points were manually inserted to the experimental data at 2% chord for the upper and lower surfaces to more accurately match the Visual Foil curve. Coefficients calculated with these additional two data points at 2% chord are denoted as adjusted coefficient values in Table 1.

By comparing these four plots of  $C_p$  vs. Chord, it can be seen that the most drastic changes in the Visual Foil pressure coefficient with respect to the angle of attack are seen in the first 20% chord for the upper surface and in the first 2.3% chord for the lower surface. This corresponds to the theoretical pressure distribution Figure 3. At 100% chord for all angles of attack, the coefficient of pressure decreases past -0.5 for both the upper and lower surfaces. The trend seen in these plots is that the local extrema of the  $C_p$  function changes drastically with respect to the angle of attack. As the angle of attack is increased from -4 degrees to 8 degrees, the local extrema seen in the first 20% chord of the upper  $C_p$  function rises from -1.0 to 2.6. The plots show that as the airflow travels past 20% chord, the pressure coefficient in the upper surface steadily decreases to -0.05. A similar but opposite trend was seen in the lower surface in the first 2.3% chord, where the local extrema decreases from 2.26 at -4 degrees to a value of -1.0 at 8 degrees angle of attack. However, past 20% chord, the low values of  $C_p$  were fairly constant. This can be explained by the relatively flat surface over this range.

## **5.2 Lift Coefficients and Drag Coefficients vs. Angle of Attack**

The lift coefficient and the drag coefficient were both calculated from the normal force coefficient, obtained previously. Figure 10 and Figure 11 show the plot of  $C_L$  or  $C_D$  vs. angle of attack for all airspeeds. The superposition of the airspeed plots on both the  $C_L$  and  $C_D$  plots allow for comparison in more detail. It can be seen that the overlapping markers of various

airspeeds confirm that the lift and drag coefficients are both independent of wind tunnel velocity. The trend seen in these two plots both suggest an increasing linear relationship in respect to the angle of attack from -4 to 8 degrees.

In addition to providing the pressure coefficient distribution, Visual Foil also gives theoretical values for the lift and drag coefficients as a function of angle of attack. The Visual Foil results were then plotted along with the experimentally obtained lift and drag coefficients in Figure 10 and Figure 11. In comparison to the experimentally obtained data, the lift coefficients from the Visual Foil showed strong agreement to the experimental data. However, the drag coefficients were not as agreeable. This error is also due to the omitted normal component in the drag force Eq. (1).

### **5.3 Pitching Moment Coefficients**

The leading edge pitching moment,  $C_{M,LE}$ , was calculated from the experimental data and is shown in Table 1. Again, the adjusted values represent the moment calculated with the two inserted data points at 2% chord. Both the experimental and theoretical values (Visfoil) of the pitching moment are shown. The theoretical values prove to be consistent with the experimentally obtained data. Table 1 illustrates that the pitching moment decreases as the angle of attack is increased and the values remain fairly constant at the three different speeds. The consistency in the values with respect to the velocity shows that the pitching moment is independent from airspeed.

## 5.4 Center of Pressure

In Table 1, the calculated values of center of pressure are shown. From this table, the trend seems to be that the center of pressure moves toward the leading edge as the angle of attack increases. This observation agrees with geometric intuition.

The experimentally obtained data points were close to the theoretical values except at an angle of attack of -4 degrees. It is observed that the theoretical value of the -4 degree center of pressure from the Visual Foil data was calculated to be 195% chord, implying that the center of pressure is physically detached from the airfoil. Due to the fact that the Visual Foil can not recognize percentage values above 100%, the value was then concluded to be incorrect.

## 5.5 Pitching Moment through the Quarter Chord Point

Also shown in Table 1 is the experimental and theoretical quarter pitching moment data points. The trend seen in the experimental  $C_{M, (c/4)}$  values is that the values increase as the angle of attack is increased. The theoretical values of  $(C_{M, (c/4)} \text{ Visfoil})$  also show that the values increase with respect to increasing angle of attack. The trends and consistency in the data also show that the quarter pitching moment is dependent of angle of attack, and independent of airspeed.

## 5.6 Wake Survey Pressure Distribution of Vertically mounted Pressure Wing

The results from the wake pressure survey measurements at angles of attack of -4, 0, 4, and 8 degrees are plotted in Figure 12, Figure 13, Figure 14, and Figure 15. The plots show the normalized wake survey pressure distribution  $q/q_\infty$  versus distance across the wake for each angle of attack for the three different velocities. The range of wake widths remains fairly constant at approximately 5 units with respect to the angle of attack; however, the position of the wake

increases with increasing angle of attack. Therefore, as the angle of attack is increased, the frontal area of the airfoil exposed to the fluid flow increases, resulting in an increase of pressure drag as more fluid is disturbed. Accordingly, Figure 12, Figure 13, Figure 14, and Figure 15 show a trend that as the angle of attack was increased, the wake moves towards the trailing edge of the airfoil.

### **5.7 Drag Coefficient from the Momentum Method**

From the momentum method, the drag coefficient for the airfoil was calculated by integrating the wake pressure distribution for each angle of attack and the three velocities. The resulting drag coefficients are recorded in Table 1, labeled as “Drag.” The drag coefficients generally increase with increasing angle of attack, with exception of -4 degrees angle of attack. Regardless of the velocity of the fluid flow, the drag coefficients are fairly consistent. Therefore, the drag experienced on the airfoil depends primarily on the orientation of the airfoil, and less significantly on velocity. As shown in the Table 1, the difference in Reynolds numbers does not seem to have a significant affect on the theoretical drag coefficient values.

### **5.8 Effect of Reynolds Number on Lift, Drag, and $\frac{1}{4}$ Chord Pitching Moment**

Lift and pitching moment coefficients from the pressure wing measurements at 4 and 8 degrees, and the drag coefficient from the wake measurements at 4 and 8 degrees were plotted with respect to Reynolds Number. These plots can be seen in Figure 16. In theory, the Reynolds Number in low-speed wind tunnels such as the one used for this experiment should not affect the lift, drag, and pitching moment. [1]. By observing Figure 16, this theory behind low speed wind tunnel testing can be clearly confirmed.

## 5.9 Interpretation of Sting Balance Data

Readings of Normal Force, Axial Force, and Pitching Moment, which was taken by the LabView Sting VI, is used to produce Figure 17. Figure 17 is then broken up into three individual plots of  $C_L$ , Figure 18;  $C_D$ , Figure 19; and  $C_M$ , Figure 20; all of which is plotted with respect to angle of attack. The Reynolds Number for the three air speeds 80, 100, and 120 mph are:  $2.10E+05$ ,  $2.62E+05$ ,  $3.14E+05$  respectively.

### 5.9.1 Lift Coefficient

Figure 18 show that the coefficient of lift depends heavily on the angle of attack, and remain consistent for the three different airspeeds. The trend seen with  $C_L$  is that for increasing angle of attack, the lift coefficient initially increases from zero linearly; followed by around angle of attack = 10 degrees, the lift coefficients taper off at approximately 1.09; then suddenly, the coefficients will drop down from approximately 1.08 to 0.78 around 14 degrees angle of attack. The airfoil is said to have *stalled* when  $C_L$  drops in this fashion [3]. In comparison to the values of the lift coefficient obtained from the airfoil pressure distribution and wake survey experiment, the force balance method gave very similar results. This comparison can be seen in Figure 21, where the coefficient of lift is plotted in respect to angle of attack for the three different methods used. The force balance method scans a larger range of angle of attack values than any other method used; and with a small range of only 12 degrees, the pressure and wake method and the visual foil lift coefficients do not capture the stall.

### 5.9.2 Drag Coefficient

The drag coefficients obtained from the force balance were plotted versus angle of attack in Figure 19. From this plot of drag coefficients, it can be observed that the angle of attack affect

the drag coefficient values and the drag coefficient is independent of the airspeed. The trend seen in Figure 19 shows that the drag coefficients increases slightly for negative angle of attack of -6 to -2 degrees and increases linearly for angle of attack of -2 to 12 degrees. Again, as seen with the lift coefficients obtained by the force balance, the drag coefficients obtained by the force balance also drops suddenly at approximately 14 degrees angle of attack. This is expected due to the interdependence of the drag coefficient and lift coefficient, and because the stall is probably occurring there. In comparison to the pressure distribution and wake survey experiment, the force balance proved to generate conflicting results. Figure 22 shows the coefficient of drag with respect to angle of attack for all three methods used. Although the values are fairly similar for negative angle of attacks, positive angle of attack shows the drag coefficients obtained by the force balance exhibiting much larger values than that of the coefficients obtained by the Visual Foil or the pressure distribution and wake data. Not only is the force balance analyzing a larger range of angle of attack, its drag coefficient calculation procedure encompasses the complete equation, rather than partial as in the pressure distribution and wake measurements. This suggests that the force balance method of calculating the drag coefficient is more accurate than any other method used.

The coefficients of pitching moment initially decrease with increasing angle of attack. As seen in Figure 20,  $C_M$  decreases linearly from a value of approximately +0.08 at -6 degrees angle of attack to a value of -0.10 at 10 degrees angle of attack. The  $C_M$  function then hits a local minima at approximately 12 degrees and because of the large range of angle of attack, the  $C_M$  function jumps up from -0.06 to +0.04 at approximately 14 degrees angle of attack. The dramatic increase results in the stall of the airfoil.  $C_M$  is relatively dependent of the speed of the air flow. Figure 20 shows that the  $C_M$  values are slightly higher for higher wind speed velocities.

## 6 Conclusion

In this experiment, the Clark-Y14 was confirmed to behave well under the range of Reynolds numbers applied. The lift drag coefficient ratio was fairly high, on the order of 10:1. Furthermore, the stall angle was calculated by sting balance to be approximately 15 degrees, giving the airfoil reasonable degree of freedom in pitch. Drag coefficients obtained from the wake survey and the force balance exhibited strong agreement, and the lift coefficients calculated from the airfoil pressure distribution and force balance were also agreeable. Furthermore, comparison between theoretical values generated by Visual Foil coincided well with the various experimentally obtained data. Strong agreement across the various testing methods provides firm reinforcement to the conclusions drawn.

However, limitations in the wind tunnel capabilities precluded testing at higher Reynolds numbers to determine the extent of effective performance by the Clark Y-14 airfoil. Furthermore, viscosity and compressibility effects were not considered in this experiment. Errors were considered to be minor, despite the calculated values from error propagation, due to likely overestimation of the numeric error. Even with these errors and limitations, it seems safe to conclude from the data acquired that aerodynamic coefficients are primarily a function of angle of attack, and that the Clark Y-14 airfoil is a strong recommendation for low-speed applications.

## 7 References

- [1] William H. Rae Jr., Alan Poe. *Low-Speed Wind Tunnel Testing*. John Wiley & Sons, Inc., second edition, 1984
- [2] John D. Anderson Jr. *Fundamentals of Aerodynamics*. McGraw-Hill, third edition, 2001
- [3] Robert W. Fox, Alan T. McDonald. *Introduction to Fluid Mechanics*. John Wiley & Sons, Inc., fifth edition, 1998
- [4] John R. Taylor. *An Introduction to Error Analysis*. University Science Books, second edition, 1997

## 8 Error Analysis

Many factors contributed to the errors found in this fluid analysis of the Clark Y-14 airfoil. The two types of uncertainty found include both systemic errors in measurements and the propagation of these uncertainties in calculated values. Each of these errors will be discussed for the calibration, pressure distribution, and force balance parts of the experiment.

### 8.1 Calibration

The main intrinsic errors found in the calibration of the wind tunnel come from the measurements recorded for the temperature and pressure. The temperature, measured in Kelvin, has an uncertainty of  $\pm 1$  K. The pressure, measured in mm Hg, has an uncertainty of  $\pm 0.1$  mm Hg. Also of importance, are the uncertainties found in the length of the airfoil,  $\pm 0.00254$  m, the viscosity of the air,  $\pm 10^{-7}$  N s / m<sup>2</sup>, and the pitot tube pressure,  $\pm 0.00254$  m H<sub>2</sub>O.

These uncertainties propagate through the equations for Reynolds number and the density of air in Eq. (14) and Eq. (15) below.

$$\rho_{\infty} = \frac{p_b M}{RT} \quad (14)$$

$$R_e = \frac{\rho V D}{\mu} \quad (15)$$

By application of the quadrature rule for products and quotients in Eq. (16) and Eq. (17) the uncertainties in these values are calculated.

$$\frac{\delta\rho_{\infty}}{\rho_{\infty}} = \sqrt{\left(\frac{\delta p_b}{p_b}\right)^2 + \left(\frac{\delta T}{T}\right)^2} \quad (16)$$

$$\frac{\delta R_e}{R_e} = \sqrt{\left(\frac{\delta\rho_{\infty}}{\rho_{\infty}}\right)^2 + \left(\frac{\delta D}{D}\right)^2 + \left(\frac{\delta\mu}{\mu}\right)^2} \quad (17)$$

In determining the uncertainty for the density of the air,  $\rho_{\infty}$ , the variables, R (universal gas constant), and M (molar mass of air), are specifically omitted because they are constants. This is also the case for V (the air velocity), which is held constant in the equation for the uncertainty of Reynolds number.

Using Eq. (18) and Eq. (19), the uncertainties can be found for each velocity; 80 mph test at -4 degrees angle of attack will be used as an example.

$$\delta\rho_{\infty} = 1.2017 \frac{\text{kg}}{\text{m}^3} \sqrt{\left(\frac{1 \text{ mm Hg}}{765 \text{ mm Hg}}\right)^2 + \left(\frac{1 \text{ K}}{295 \text{ K}}\right)^2} = \pm 0.004366 \frac{\text{kg}}{\text{m}^3} \quad (18)$$

$$\delta R_e = 211092.44 \sqrt{\left(\frac{0.004366 \frac{\text{kg}}{\text{m}^3}}{1.2017 \frac{\text{kg}}{\text{m}^3}}\right)^2 + \left(\frac{0.00254 \text{ m}}{0.0889 \text{ m}}\right)^2 + \left(\frac{0.0000001 \frac{\text{kg}}{\text{m} \cdot \text{s}}}{0.0000181 \frac{\text{kg}}{\text{m} \cdot \text{s}}}\right)^2} = \pm 6190.63 \quad (19)$$

The significance of these uncertainties can be observed by calculating the percent error in each value as seen in Eq. (20) and Eq. (21).

$$\frac{\delta\rho_{\infty}}{\rho_{\infty}} = \frac{0.004366 \frac{\text{kg}}{\text{m}^3}}{1.2017 \frac{\text{kg}}{\text{m}^3}} = 0.36\% \quad (20)$$

$$\frac{\delta \text{Re}}{\text{Re}} = \frac{6190.63}{211092.44} = 2.9\% \quad (21)$$

These values for percent error in the air density and Reynolds number are small and therefore deemed acceptable for this experiment.

## 8.2 Pressure Distribution

There were two main sources of error involved in calculating aerodynamic coefficients from pressure data. One error was that a numerical truncation error due to approximating a continuous curve (Eq. (22)) with a summation, and the other error was the uncertainty in measured values.

$$C_N = \frac{1}{c} \int_0^c (C_{pL} - C_{pU}) dx \quad (22)$$

By replacing the integral equation for the normal force coefficient (Eq. (22)), with a trapezoidal approximation, a numerical error is introduced into the results. This numerical error may be approximated by using a second order Runge-Kutta method to calculate the second derivative at each point and then finding the error due to overestimation and underestimation intrinsic to the trapezoidal rule. However, for the scope of this paper, it was assumed that the numerical error of the trapezoidal rule is minor compared to the random errors involved in measurement of experimental data. This assumption was made on the basis that the pressure distribution is a well behaved, smooth function that is well approximated as long as the data points are spaced closely enough to capture the sharp changes. This criterion was reasonably satisfied by both the spacing interval over the chord.

To propagate random error due to measurement, random errors from measured data is summed in quadrature to yield error in the aerodynamic coefficients. The coefficients  $C_{p,U}$  and

$C_{P,L}$  are calculated from uncertain values of local pressure and dynamic pressure and are thus uncertain as well (Eq. (23)).

$$\frac{\delta C_{P,U}}{C_{P,U}} \approx \frac{\delta C_{P,L}}{C_{P,L}} \approx \sqrt{\left(\frac{\delta q_\infty}{q_\infty}\right)^2 + \left(\frac{\delta p}{p}\right)^2} \quad (23)$$

In these equations, the coefficients and pressure are local to each data location, while the dynamic pressure is at freestream. In order to obtain the error in dynamic pressure, it was necessary to compare data across different angles of attack at the same flow velocity. The difference between the high and low values was then considered the extent of error, and  $\delta q_\infty$  was assigned half of that value. These local coefficients were then used to calculate  $C_N$ . The error for  $C_N$  must be taken at each point, and then the combined error is summed in quadrature for a total  $C_N$  error (Eq. (24)) and (Eq. (25)).

$$\delta C_{N,i} = \sqrt{(\delta C_{P,U})^2 + (\delta C_{P,L})^2} \quad (24)$$

$$\delta C_N \approx \sqrt{\sum_{i=0}^{i=n} (\delta C_{N,i})^2} \quad (25)$$

The value of  $C_N$  is then used to calculate the aerodynamic coefficients by trigonometric relations (Eq. (1)). However, the error in the moment coefficients must be considered differently, since the midpoint approximation used was not a random statistical error. Instead, an alternative implementation is to do a worst case percentage error for each point, and then sum the percentages in quadrature to yield a total percent error (Eq. (28)).

$$\delta C_L \approx \sqrt{\left(\frac{\partial C_L}{\partial C_N} \delta C_N\right)^2 + \left(\frac{\partial C_L}{\partial \alpha} \delta \alpha\right)^2} \quad (26)$$

$$\delta C_D \approx \sqrt{\left(\frac{\partial C_D}{\partial C_N} \delta C_N\right)^2 + \left(\frac{\partial C_D}{\partial \alpha} \delta \alpha\right)^2} \quad (27)$$

$$\frac{\delta C_{M,ref}}{C_{M,ref}} \approx \sqrt{\left(\frac{\delta C_{N,i}}{C_{N,i}} + \frac{\delta x_i}{x_i}\right)^2 + \dots + \left(\frac{\delta C_{N,n}}{C_{N,n}} + \frac{\delta x_n}{x_n}\right)^2} \quad (28)$$

By considering the measurements acquired at 80 mph, -4 degrees angle of attack, numerical approximations to these expressions may be obtained. Numerical error in using the midpoint between data points was treated as random error in order to simplify analysis, but the resulting error values were not agreeable. The error in lift, drag, and normal force coefficients were 25.76%, 28.62%, and 25.76% respectively. The similar percentage error was due to the constant percent error applied to all pressure data measurements. The moment coefficients returned an error of approximately 25.03% when the numerical error in x was approximated by a random error variance of 0.05.

### 8.3 Wake Survey

The errors involved in performing the wake survey are similar to the errors obtained by pressure distribution calculations. In the wake survey method, all values were normalized by the upstream pressure, resulting in statistically insignificant error at the entrance of the control volume, while the errors at the exit of the control volume were due to the error in rake measurement and the error in freestream pressure. These values may be calculated by the use of Eq. (29) and Eq. (30).

$$\chi = \frac{q}{q_\infty} \quad (29)$$

$$\frac{\delta\chi}{\chi} = \sqrt{\left(\frac{\delta q}{q}\right)^2 + \left(\frac{\delta q_\infty}{q_\infty}\right)^2} \quad (30)$$

The normalized dynamic pressure  $\chi$  was used instead of the velocity profile in order to calculate drag. Accordingly, the momentum conservation equation was rewritten to accommodate this substitution. Once again, the integral term was approximated with a summation, and numerical error was introduced. As before, this was neglected in order to focus on measurement error. With these considerations, the error in drag coefficient may be represented by Eq. (31).

$$\delta C_D = \sqrt{\sum_i^n (\delta\chi_i)^2} \quad (31)$$

The error in dynamic pressure at each point was taken to be random and summed in quadrature to yield an expression for error in drag coefficient. By propagating this error for the data gathered at 80 mph at -4 degrees angle of attack, the estimated error in drag coefficient was 22.31%.

#### 8.4 Force Balance

The errors involved in estimating the normal force, axial force, and pitching moment (9) acting on the airfoil from the values recorded by the sting balance are random errors and propagated in quadrature with partial derivatives as a weighing function (Eq. (32)), (Eq. (33)), and (Eq. (34)).

$$\delta N \approx \sqrt{\left(\frac{\partial N}{\partial N'} \delta N'\right)^2 + \left(\frac{\partial N}{\partial A'} \delta A'\right)^2 + \left(\frac{\partial N}{\partial P'} \delta P'\right)^2} \quad (32)$$

$$\delta A \approx \sqrt{\left(\frac{\partial A}{\partial N'} \delta N'\right)^2 + \left(\frac{\partial A}{\partial A'} \delta A'\right)^2 + \left(\frac{\partial A}{\partial P'} \delta P'\right)^2} \quad (33)$$

$$\delta P \approx \sqrt{\left(\frac{\partial P}{\partial N'} \delta N'\right)^2 + \left(\frac{\partial P}{\partial A'} \delta A'\right)^2 + \left(\frac{\partial P}{\partial P'} \delta P'\right)^2} \quad (34)$$

By inserting values from the empirical correlation equations, and dropping the lower order terms, one arrives at a numeric expression of error (Eq. (35)), (Eq. (36)), and (Eq. (37)). These expressions show that the error in the normal force on the wing is most closely related to the error in the measured normal force of the sting balance, and likewise for the axial force and pitching moment. This confirms that the empirical correlations (9) are correction factors and errors in the correcting terms are insignificant.

$$\delta N \approx .9504 \delta N' \quad (35)$$

$$\delta A \approx .5912 \delta A' \quad (36)$$

$$\delta P \approx 1.182 \delta P' \quad (37)$$

Additional errors are introduced as these corrected values converted into aerodynamic forces and nondimensionalized into lift, drag, and pitching moment coefficients. From the trigonometric equations of lift and drag the errors may be propagated in quadrature.

$$\delta F_L \approx \sqrt{\left(\frac{\partial F_L}{\partial N} \delta N\right)^2 + \left(\frac{\partial F_L}{\partial A} \delta A\right)^2 + \left(\frac{\partial F_L}{\partial \alpha} \delta \alpha\right)^2} \quad (38)$$

$$\delta F_D \approx \sqrt{\left(\frac{\partial F_D}{\partial N} \delta N\right)^2 + \left(\frac{\partial F_D}{\partial A} \delta A\right)^2 + \left(\frac{\partial F_D}{\partial \alpha} \delta \alpha\right)^2} \quad (39)$$

$$\delta M \approx \sqrt{\left(\frac{\partial M}{\partial P} \delta P\right)^2 + \left(\frac{\partial M}{\partial N} \delta N\right)^2 + \left(\frac{\partial M}{\partial D} \delta D\right)^2 + \left(\frac{\partial M}{\partial X} \delta X\right)^2} \quad (40)$$

In the moment error equation, M represents the moment about a given reference point, D is the distance to the reference point, and X is the distance to the balance center. From the values of lift, drag and pitching moments, an error analysis of Eq. (5), Eq. (6), and Eq. (8) was done to derive Eq. (41), Eq. (42), and Eq. (43). However, an order analysis would reveal that error in the area and chord are minor compared to errors introduced by the dynamic pressure and aerodynamic forces. Thus, these terms may be safely removed from the estimate of error.

$$\frac{\delta C_L}{C_L} \approx \sqrt{\left(\frac{\delta F_L}{F_L}\right)^2 + \left(\frac{\delta q_\infty}{\delta q_\infty}\right)^2} \quad (41)$$

$$\frac{\delta C_D}{C_D} \approx \sqrt{\left(\frac{\delta F_D}{F_D}\right)^2 + \left(\frac{\delta q_\infty}{\delta q_\infty}\right)^2} \quad (42)$$

$$\frac{\delta C_{M,ref}}{C_{M,ref}} \approx \sqrt{\left(\frac{\delta M_{ref}}{M_{ref}}\right)^2 + \left(\frac{\delta q_\infty}{\delta q_\infty}\right)^2} \quad (43)$$

## 9 Appendix

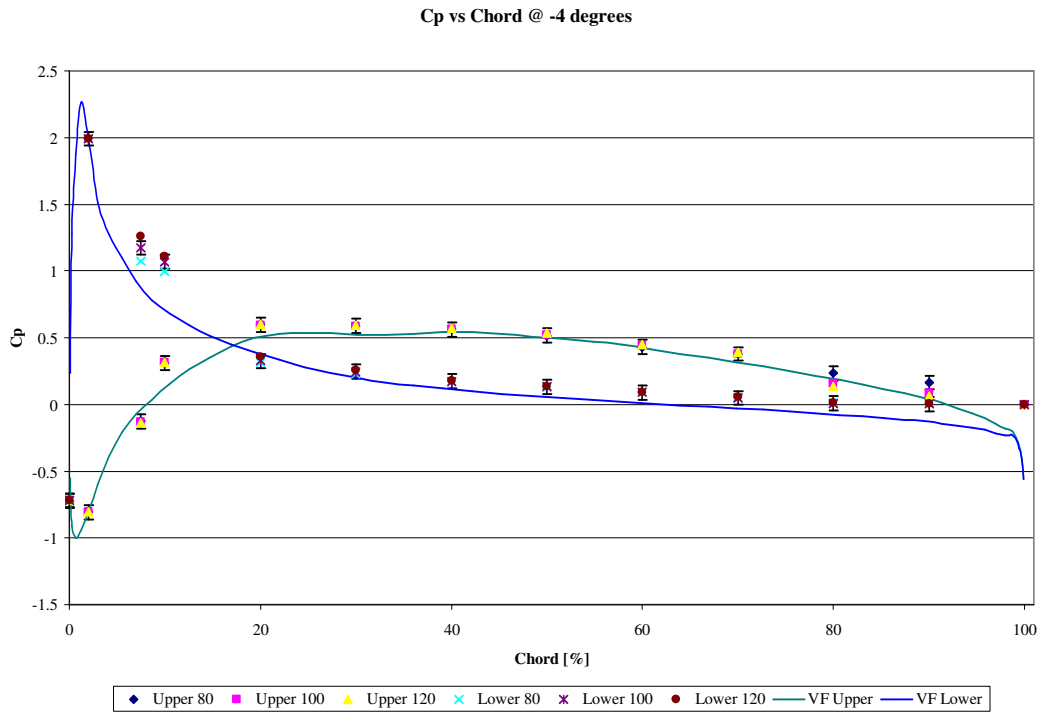
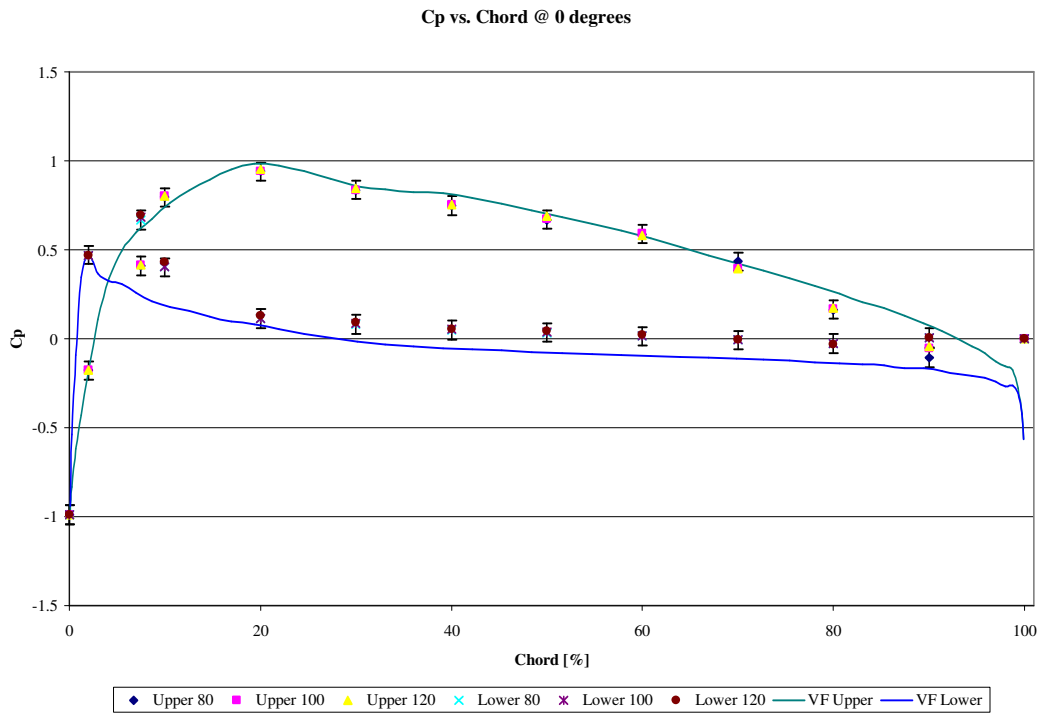
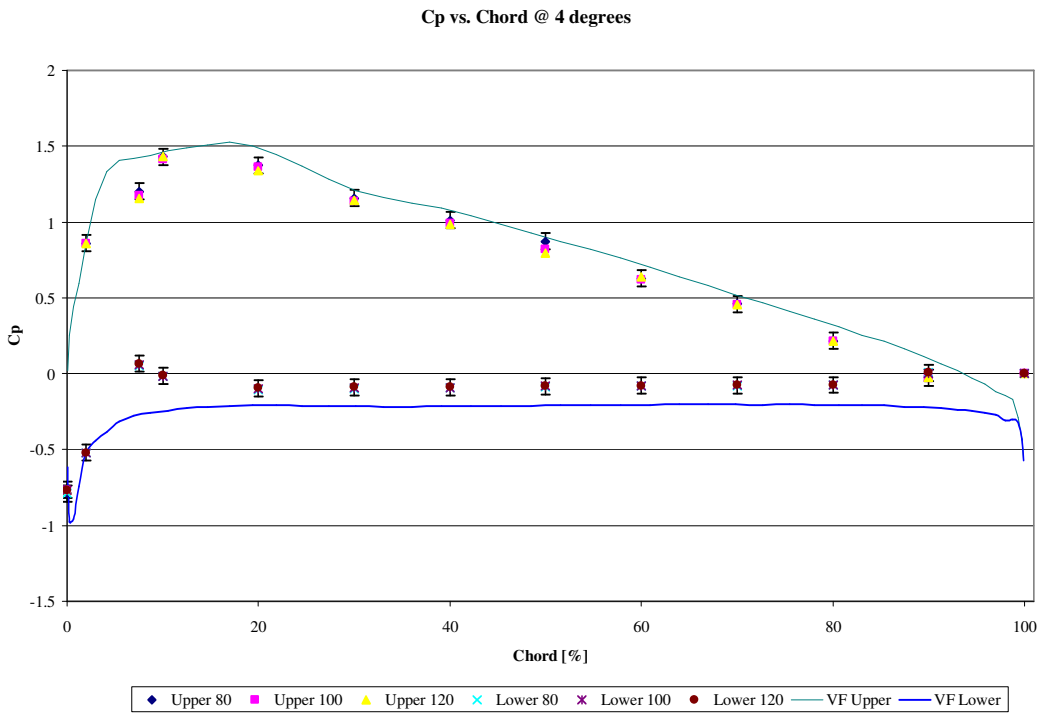


Figure 6



**Figure 7**



**Figure 8**

Cp vs. Chord @ 8 degrees

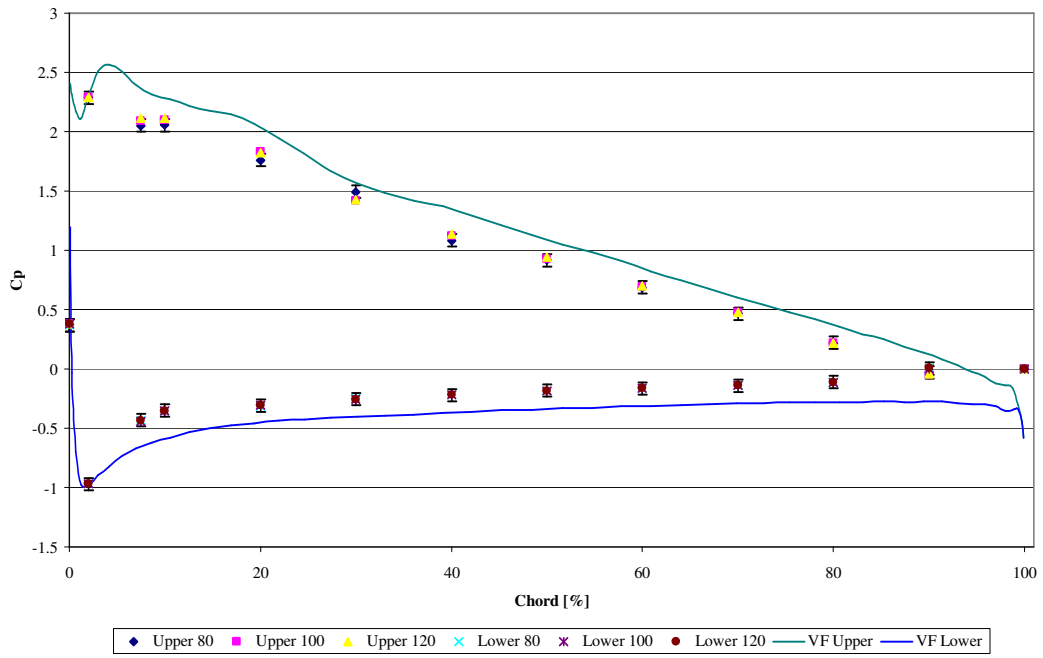


Figure 9

Cl vs. AoA

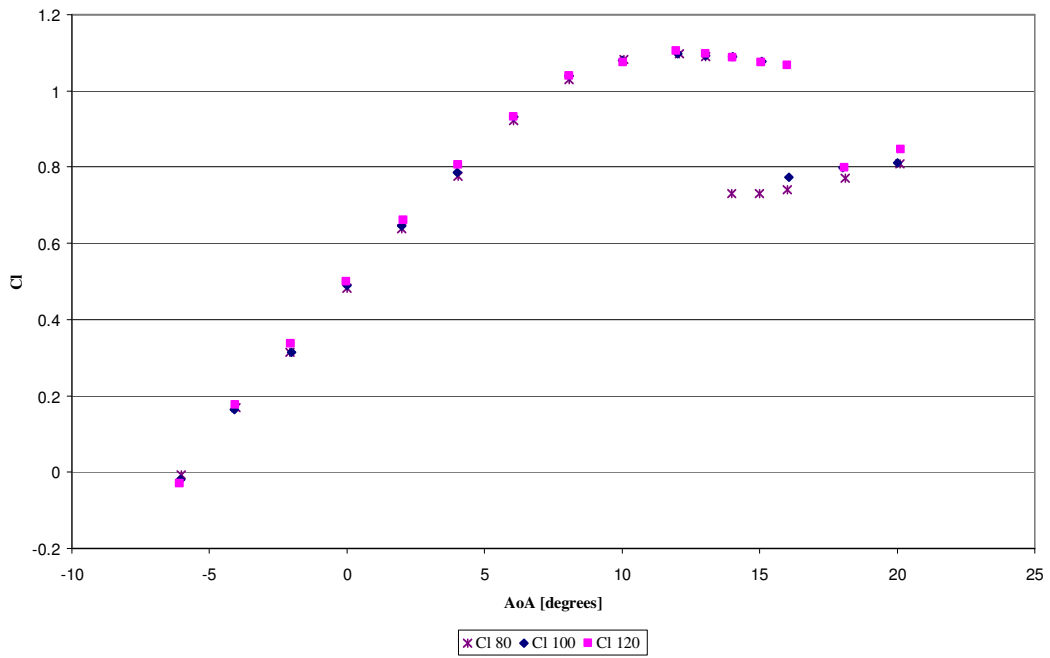
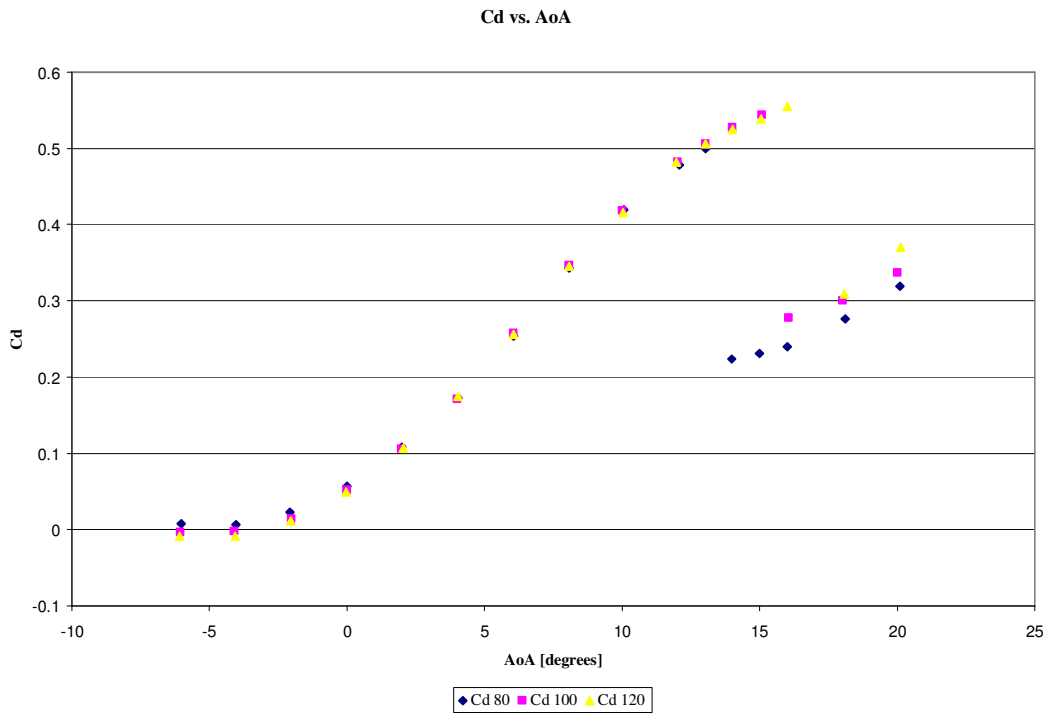
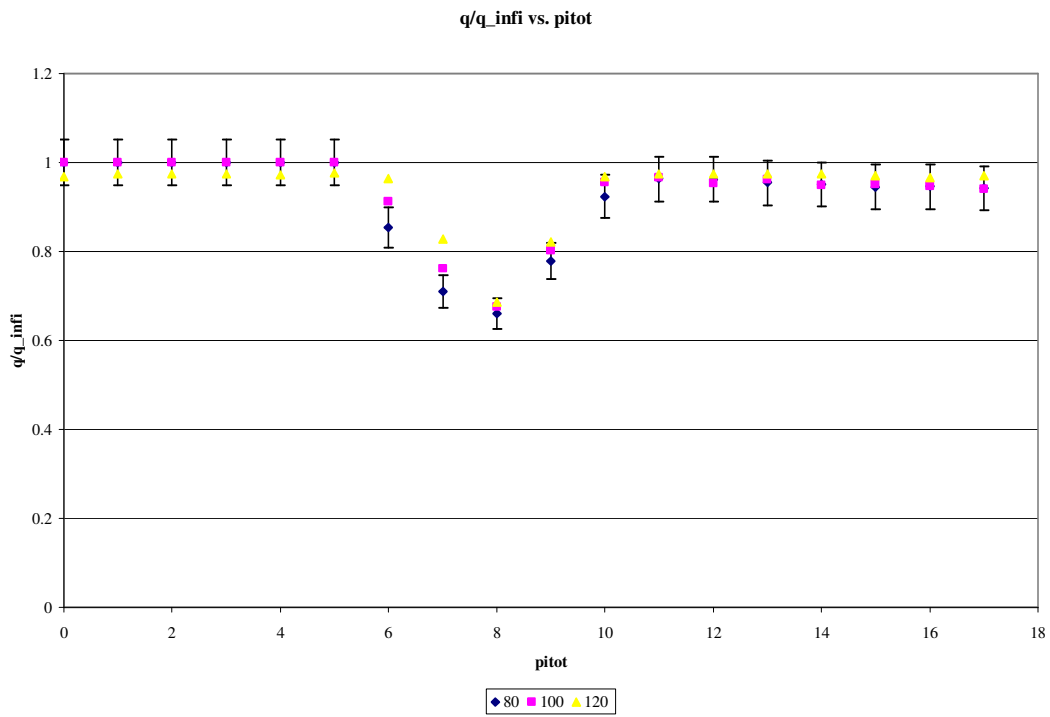


Figure 10



**Figure 11**



**Figure 12**

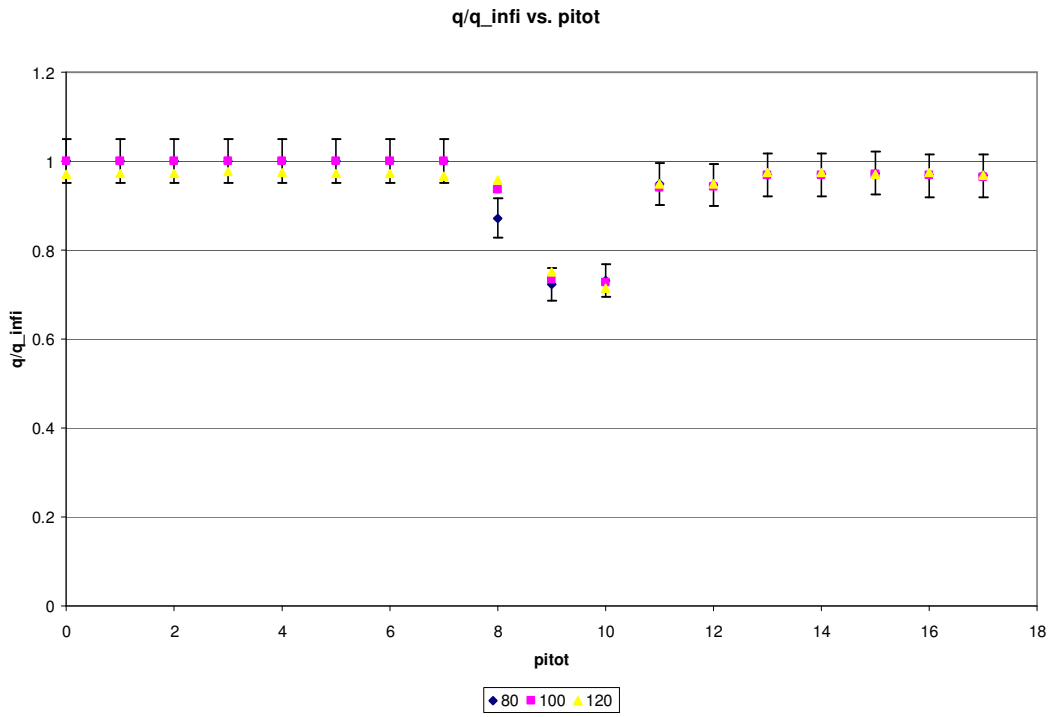


**Figure 13**

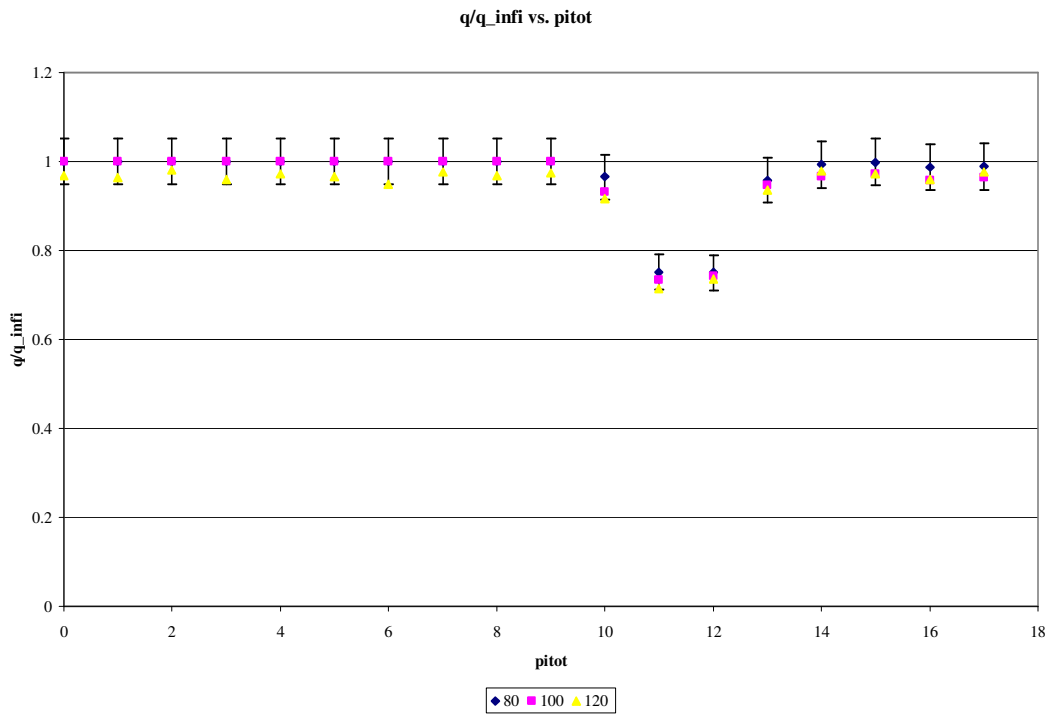


**Figure 14**

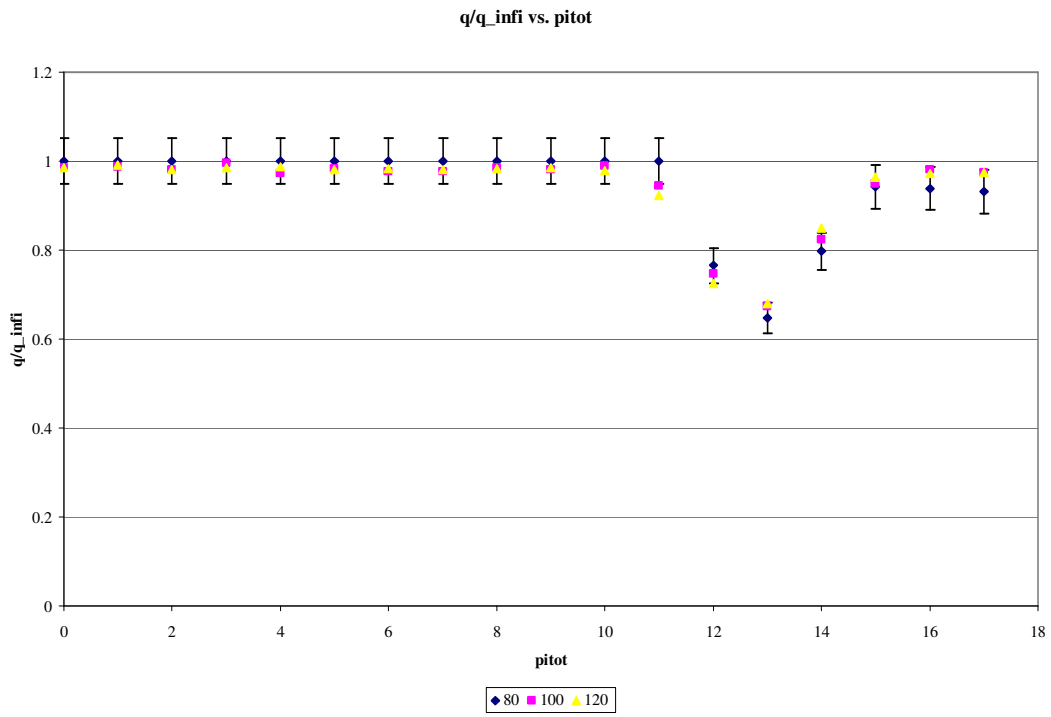


**Figure 15**

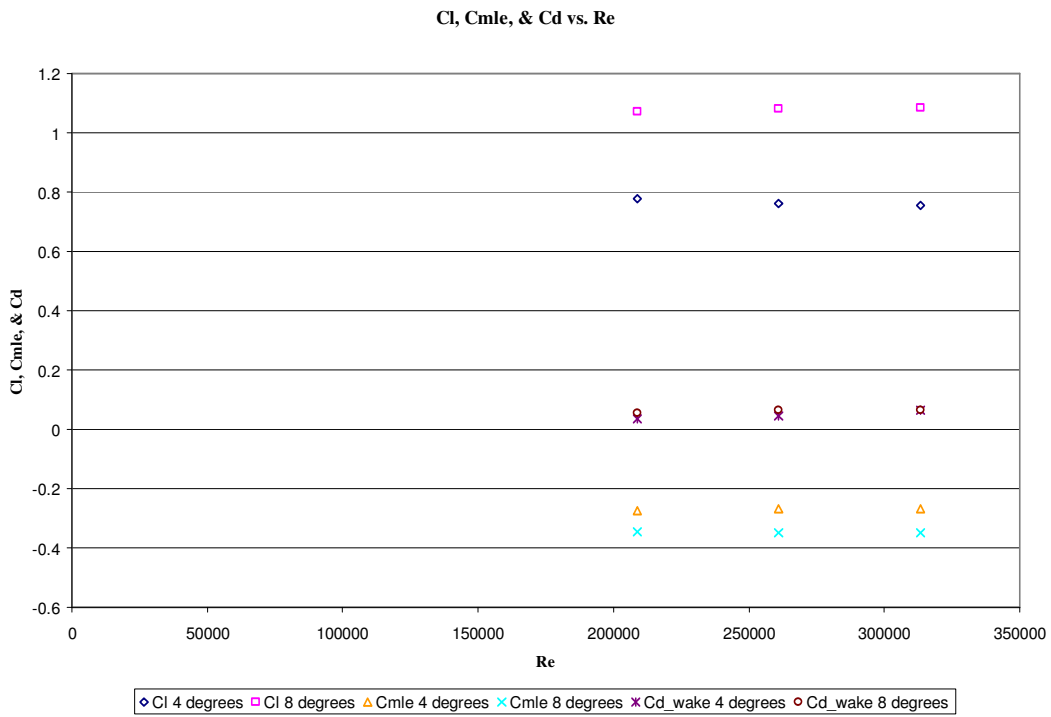


**Figure 16**

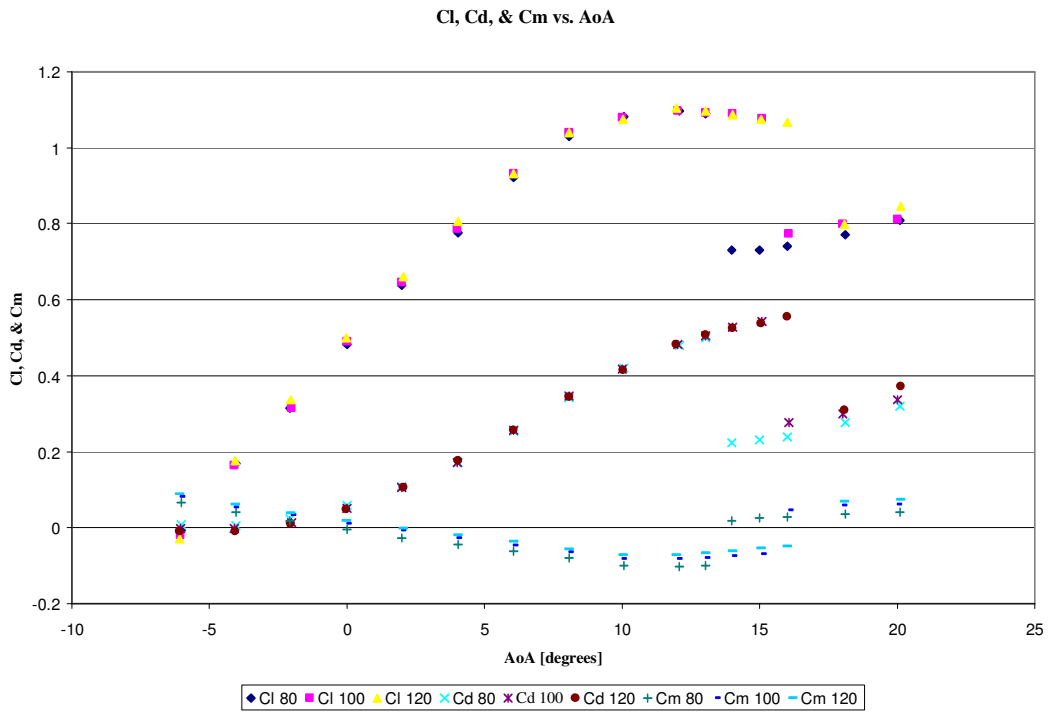


**Figure 17**

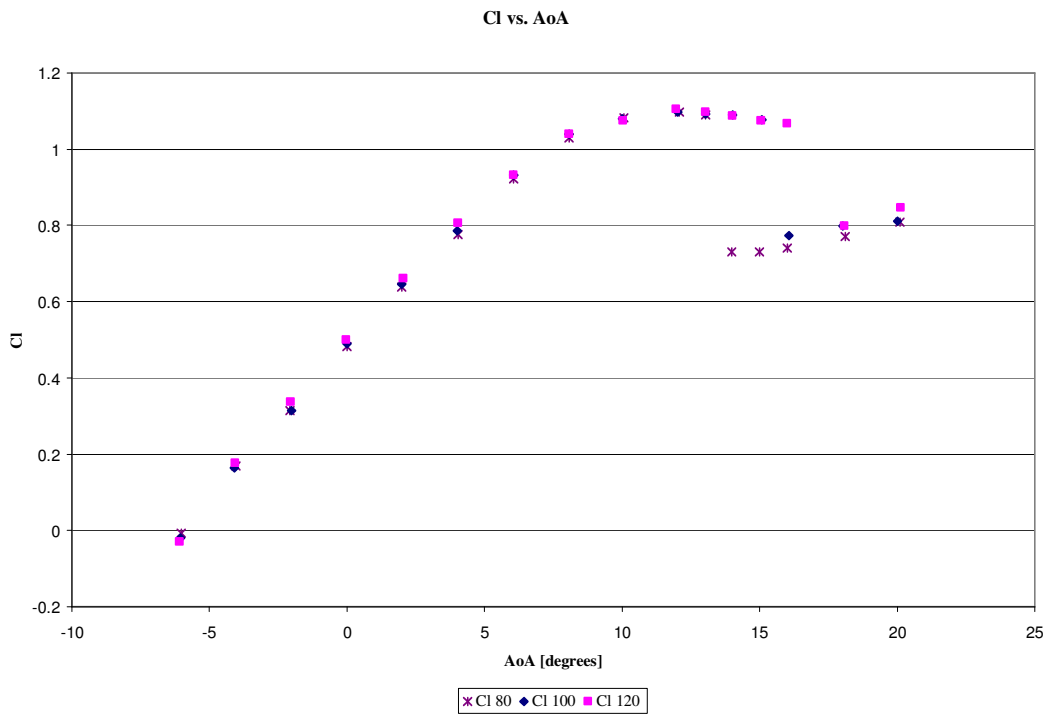


**Figure 18**

**Cd vs. AoA**

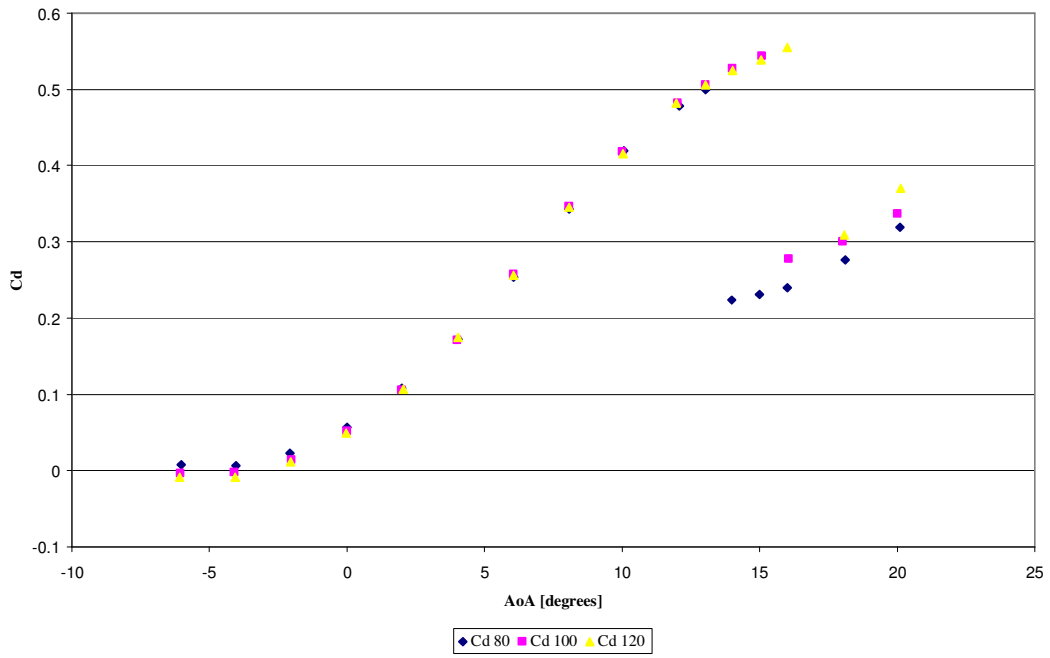


**Figure 19**

**Cm vs. AoA**

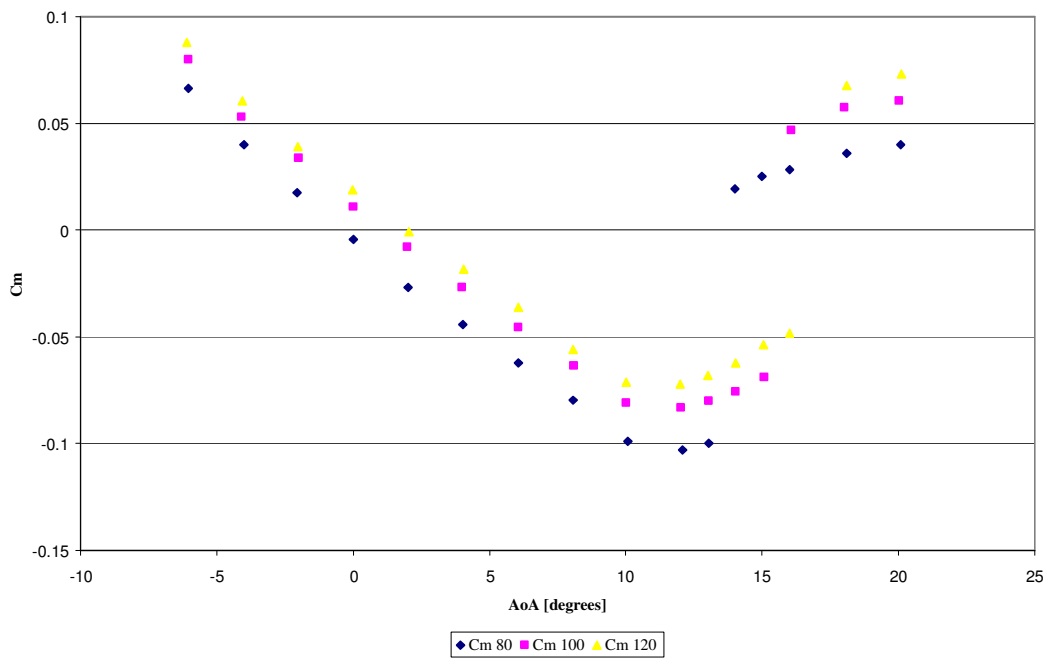


**Figure 20**

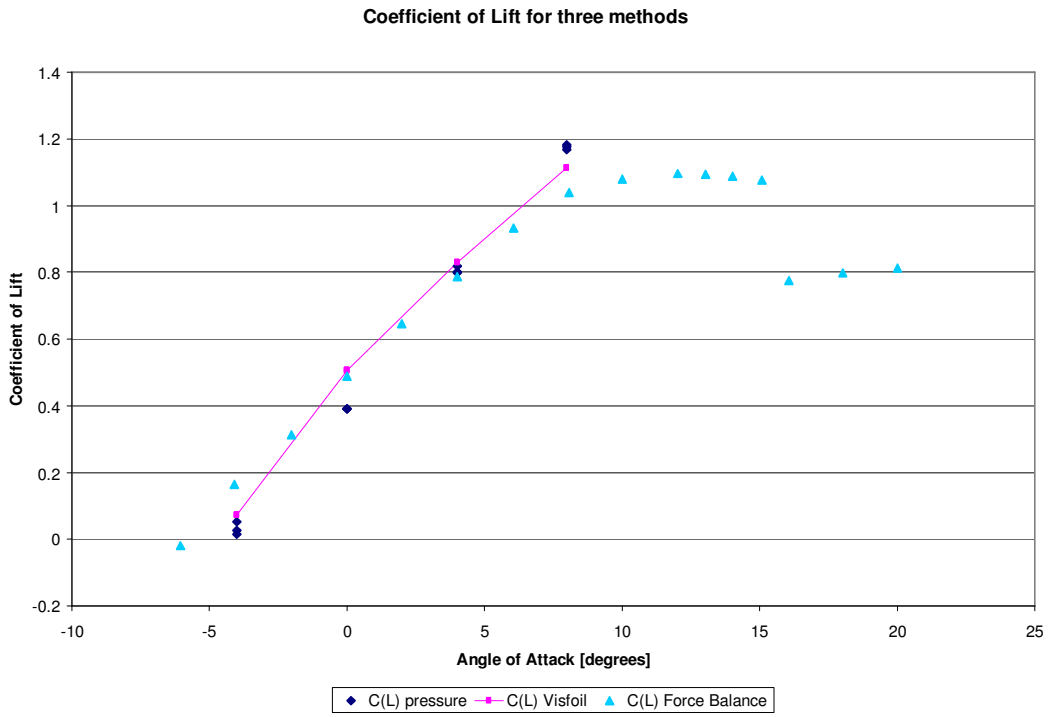


**Figure 21**

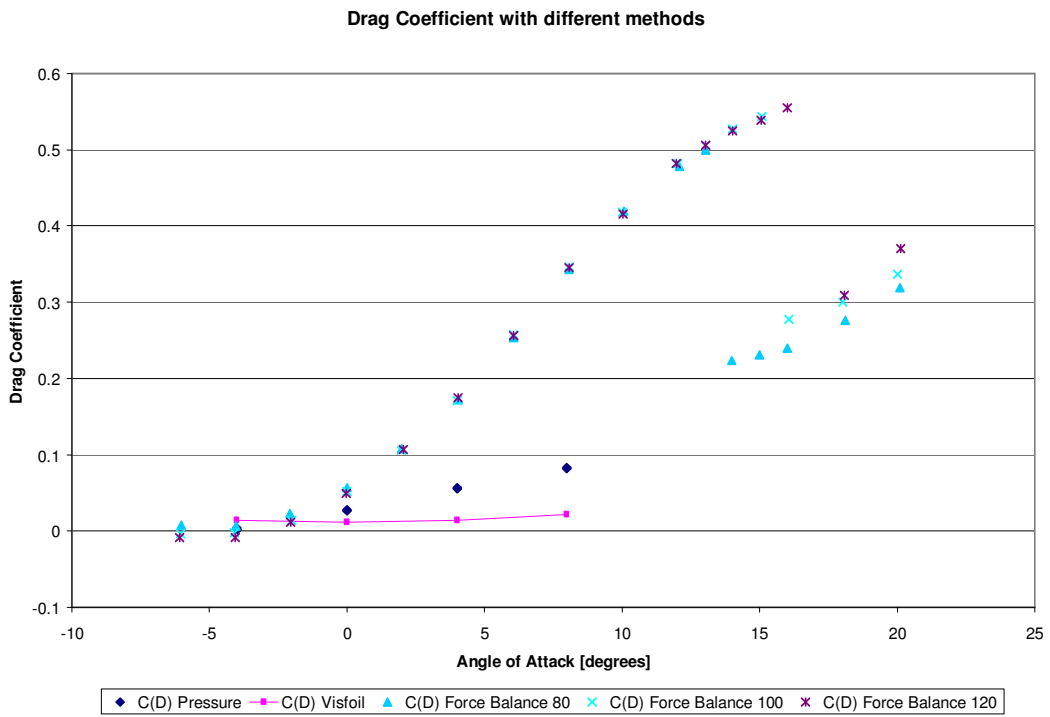


**Figure 22**

	-4 degrees			0 degrees		
	80	100	120	80	100	120
Cn	0.145	0.117	0.106	0.413	0.414	0.413
Cl	0.144	0.117	0.106	0.412	0.413	0.412
Cl_adjusted	0.0518409	0.0253381	0.0151172	0.3897944	0.3911134	0.3907637
Cl VisFoil	0.073	0.073	0.073	0.506	0.506	0.506
Cd	0.010	0.008	0.007	0.029	0.029	0.029
Cd_adjusted	0.0036251	0.0017718	0.0010571	0.0272571	0.0273493	0.0273249
Cd VisFoil	0.015	0.015	0.015	0.012	0.012	0.012
Drag	0.081	0.071	0.062	0.054	0.051	0.060
Cmle	-0.118	-0.104	-0.101	-0.172	-0.175	-0.176
Cmle_adjusted	-0.105684	-0.092866	-0.089652	-0.150351	-0.152799	-0.15405
Cmle VisFoil	-0.142	-0.142	-0.142	-0.242	-0.242	-0.242
Cm(c/4)	-0.118	-0.104	-0.100	-0.171	-0.174	-0.175
Cm(c/4)_adjusted	-0.105554	-0.092802	-0.089614	-0.149374	-0.151819	-0.153071
Cm(c/4) VisFoil	-0.123	-0.123	-0.123	-0.115	-0.115	-0.115
Xcp [%]	82	89	95	42	42	43
Xcp [%]_adjusted	203.36582	365.61456	591.6009	38.477909	38.972515	39.326788
Xcp VisFoil [%]	195	195	195	48	48	48
Reynolds	2.111E+05	2.639E+05	3.166E+05	2.088E+05	2.611E+05	3.133E+05
	4 degrees			8 degrees		
	80	100	120	80	100	120
Cn	0.779	0.762	0.758	1.073	1.083	1.088
Cl	0.777	0.760	0.756	1.070	1.080	1.085
Cl_adjusted	0.8169833	0.800346	0.7966018	1.167178	1.1771041	1.1815151
Cl VisFoil	0.828	0.828	0.828	1.112	1.112	1.112
Cd	0.054	0.053	0.053	0.075	0.076	0.076
Cd_adjusted	0.057129	0.0559656	0.0557038	0.081617	0.0823111	0.0826196
Cd VisFoil	0.015	0.015	0.015	0.021	0.021	0.021
Drag	0.035	0.045	0.065	0.056	0.063	0.063
Cmle	-0.275	-0.269	-0.269	-0.345	-0.347	-0.348
Cmle_adjusted	-0.240247	-0.234513	-0.234254	-0.29964	-0.30089	-0.302145
Cmle VisFoil	-0.308	-0.308	-0.308	-0.370	-0.370	-0.370
Cm(c/4)	-0.274	-0.267	-0.267	-0.342	-0.344	-0.346
Cm(c/4)_adjusted	-0.2382	-0.232507	-0.232257	-0.296715	-0.29794	-0.299184
Cm(c/4) VisFoil	-0.101	-0.101	-0.101	-0.092	-0.092	-0.092
Xcp [%]	35	35	35	32	32	32
Xcp [%]_adjusted	29.335025	29.230018	29.334979	25.609618	25.499653	25.510375
Xcp VisFoil [%]	37	37	37	33	33	33
Reynolds	2.088E+05	2.611E+05	3.133E+05	2.088E+05	2.611E+05	3.133E+05

Table 1